



HAL
open science

Influence of ultra-low ethylene partial pressure on microstructural and compositional evolution of sputter-deposited Zr-C thin films

Hicham Zaid, Angel Aleman, Koichi Tanaka, Chao Li, Pascal Berger, Tyson Back, Joshua Fankhauser, Mark S. Goorsky, Suneel Kodambaka

► **To cite this version:**

Hicham Zaid, Angel Aleman, Koichi Tanaka, Chao Li, Pascal Berger, et al.. Influence of ultra-low ethylene partial pressure on microstructural and compositional evolution of sputter-deposited Zr-C thin films. *Surface and Coatings Technology*, 2020, 398, pp.126053. 10.1016/j.surfcoat.2020.126053 . cea-02884587

HAL Id: cea-02884587

<https://cea.hal.science/cea-02884587>

Submitted on 30 Jun 2020

HAL is a multi-disciplinary open access archive for the deposit and dissemination of scientific research documents, whether they are published or not. The documents may come from teaching and research institutions in France or abroad, or from public or private research centers.

L'archive ouverte pluridisciplinaire **HAL**, est destinée au dépôt et à la diffusion de documents scientifiques de niveau recherche, publiés ou non, émanant des établissements d'enseignement et de recherche français ou étrangers, des laboratoires publics ou privés.

1 **Influence of ultra-low ethylene partial pressure on microstructural and compositional**
2 **evolution of sputter-deposited Zr-C thin films**

3
4 Hicham Zaid^{a,*}, Angel Aleman^b, Koichi Tanaka^a, Chao Li^a, Pascal Berger^c, Tyson Back^d, Josh
5 Fankhauser^a, Mark S. Goorsky^a, and Suneel Kodambaka^a

6
7 ^a Department of Materials Science and Engineering, University of California Los Angeles, 410
8 Westwood Plaza, Los Angeles, CA 90095 USA

9 ^b Department of Mechanical and Aerospace Engineering, University of California Los Angeles,
10 420 Westwood Plaza, Los Angeles, CA 90095 USA

11 ^c Université Paris-Saclay, CEA, CNRS, NIMBE, 91191, Gif-sur-Yvette, France

12 ^d Air Force Research Laboratory, Wright Patterson AFB, OH 45433-7707

13
14 *email: hizaid@ucla.edu

15
16 **Abstract**

17 Zr-C thin films are grown on single-crystalline MgO(001) substrates via ultra-high vacuum dc
18 magnetron sputtering of Zr target in 10 mTorr Ar-C₂H₄ gas mixtures with ethylene partial
19 pressures ($p_{\text{C}_2\text{H}_4}$) between 2×10^{-7} Torr and 2×10^{-4} Torr at substrate temperature $T_s = 923$ K and
20 using $p_{\text{C}_2\text{H}_4} = 2 \times 10^{-6}$ Torr at $723 \text{ K} \leq T_s \leq 1123 \text{ K}$. The as-deposited layer microstructure and
21 composition are determined using X-ray diffraction, transmission electron microscopy, and X-ray
22 photoelectron spectroscopy. We find that the layers sputter-deposited at $T_s = 923$ K using the
23 lowest $p_{\text{C}_2\text{H}_4} = 2 \times 10^{-7}$ Torr are polycrystalline, close-packed hexagonal structured Zr:C solid
24 solutions. At higher $p_{\text{C}_2\text{H}_4} = 2 \times 10^{-6}$ Torr and 2×10^{-5} Torr, we obtain films composed of free-
25 carbon (C) and NaCl-structured ZrC_x, $x \leq 1$. The amount of C increases 104% with ten-fold
26 increase in $p_{\text{C}_2\text{H}_4}$ from 2×10^{-6} Torr to 2×10^{-5} Torr. At the highest $p_{\text{C}_2\text{H}_4} = 2 \times 10^{-4}$ Torr, the
27 layers are X-ray amorphous with ~ 49 at.% C. Films grown at $723 \text{ K} \leq T_s \leq 1123 \text{ K}$ using
28 constant $p_{\text{C}_2\text{H}_4} = 2 \times 10^{-6}$ Torr exhibit qualitatively similar microstructures, irrespective of T_s ,
29 composed of dense columnar ZrC_x grains surrounded by C and corrugated surfaces. Our results
30 suggest that the compositional and microstructural evolution of Zr-C films during reactive

31 sputter-deposition of Zr is highly sensitive to ethylene partial pressure, with as little as 0.02% of
32 the total pressure sufficient at $T_s \geq 723$ K to obtain ZrC_x films.

33 **Keywords:** transition-metal carbides, reactive magnetron sputtering, Zr-C thin films

34 1. Introduction

35 Group 4 to 6 transition-metal carbides (TMCs) are highly refractory compounds with
36 excellent thermomechanical and thermochemical properties due to a mixture of ionic, covalent,
37 and metallic bonds between the metal cations and carbon anions. Among the TMCs, ZrC
38 crystallizes in B1 (rock salt) structure ($Fm\bar{3}m$; space group 225) with a bulk lattice parameter $a_0 =$
39 0.4693 nm at room temperature [1]. ZrC is a hard (> 25 GPa), high elastic modulus (> 350 GPa),
40 and high melting point (> 3673 K) solid with good thermal (20.5 W/m.K at 293 K) and electrical
41 conductivities (2326 S/m at 293 K) and excellent resistance to wear, corrosion, and oxidation [2].
42 ZrC is used as hard protective coatings on cutting tools [3–7], as structural components in
43 aerospace vehicles, as coating material for nuclear fuel in nuclear reactors [2,3,8–11], and as
44 field-emission cathodes in electronic devices [12].

45 ZrC thin films have been grown via reactive sputtering of elemental Zr in hydrocarbon/Ar
46 gas mixtures [3,13], sputtering of compound ZrC [14,15] and Zr and C targets [16] in pure Ar
47 discharges, sol-gel synthesis [17], chemical vapor deposition [18–20], and pulsed laser deposition
48 [21,22]. Among all these techniques, reactive sputter-deposition has been the most commonly
49 used method to grow ZrC and other TMC thin films [3,13,16,23–28]. In this approach, one can
50 control both the thin film composition and the growth rate by appropriate choice of the reactive
51 gas and its flux [29]. The TMC coatings deposited via this technique typically result in two-phase
52 mixtures, composed of TMC crystallites and free-carbon (C) [3,24,27], with reactive gas
53 pressure-dependent TMC and C phase fractions, crystallinity, and mechanical properties
54 [3,24,26,27,30]. Recently, Tanaka *et al.* [31] have demonstrated tunability of Ta-C phase
55 composition in thin films sputter-deposited with ultra-low amounts of ethylene partial pressures,
56 $p_{C_2H_4}$ (0.0025 ~ 2.5% of total pressure) using a compound TaC target. Here, we focus on the

57 microstructural and compositional evolutions of thin films deposited by sputtering elemental Zr
58 target using similarly low $p_{\text{C}_2\text{H}_4}$ between 0.002 and 2% of the total pressure.

59 In this paper, we report on the effects of $p_{\text{C}_2\text{H}_4}$ (between 2×10^{-7} Torr and 2×10^{-4} Torr) and
60 substrate temperature ($723 \text{ K} \leq T_s \leq 1123 \text{ K}$) on the composition and crystallinity of Zr-
61 C/MgO(001) thin films sputter-deposited in 10 mTorr Ar-C₂H₄ gas mixtures. (Here, and in the
62 following sections, we use Zr-C to refer to both Zr:C solid solutions and ZrC_x, $x \leq 1$,
63 compounds.) Using X-ray diffraction (XRD), transmission electron microscopy (TEM), and X-
64 ray photoelectron spectroscopy (XPS), we characterized the as-deposited layer microstructure and
65 composition. We find that the films sputter-deposited at $T_s = 923 \text{ K}$ using $p_{\text{C}_2\text{H}_4} = 2 \times 10^{-7}$ Torr
66 are polycrystalline with primarily hexagonal close-packed (hcp) Zr:C solid solutions. At $p_{\text{C}_2\text{H}_4} =$
67 2×10^{-6} Torr and 2×10^{-5} Torr, the films are composed of a two-phase mixture of B1-structured
68 ZrC_x and C with an increasing phase fraction of C with increasing $p_{\text{C}_2\text{H}_4}$. At $p_{\text{C}_2\text{H}_4} = 2 \times 10^{-4}$ Torr,
69 the film is X-ray amorphous and with a high C content. The Zr-C layers sputter-deposited with
70 $p_{\text{C}_2\text{H}_4} = 2 \times 10^{-6}$ Torr at T_s between 723 K and 1123 K are all two-phase mixtures of B1-ZrC_x and
71 C with little changes in the C content with increasing T_s . Our experiments reveal that the carbon
72 content in reactively sputter-deposited Zr-C thin films is highly sensitive to the reactive gas
73 pressure.

74

75 2. Experimental details

76 All the Zr-C films are grown on single-side polished $0.5 \times 2 \times 10 \text{ mm}^3$ rectangular strips of
77 MgO(001) substrates in a custom-designed ultra-high vacuum (UHV, base pressure $< 5.3 \times 10^{-9}$
78 Torr) deposition system following the procedure described in Ref. [32]. Briefly, the MgO(001)
79 substrates are cut from $0.5 \times 10 \times 10 \text{ mm}^3$, 99.95% pure crystals (purchased from MTI), cleaned

80 via sonication sequentially in acetone, isopropyl alcohol, and deionized water, and oven-baked in
81 air at 523 K for one hour. The samples are mounted on a pyrolytic boron nitride heating stage
82 [33], where they are held by Mo clips, transferred to the main chamber, and degassed by
83 resistively heating to and holding at 1273 K until the chamber pressure is below 6×10^{-9} Torr.
84 The sample temperature T_s is then set to the desired value. In our experiments, we estimate that
85 the maximum variation in T_s across the substrate is ± 100 K. The magnetron sputter-deposition is
86 carried out using a 3.2-mm-thick \times 50.8 mm diameter Zr target (99.91 wt.% pure with 0.08 wt.%
87 Hf from ACI Alloys, Inc.), located at about 30 cm directly above the substrate. The chamber is
88 first filled with ethylene (99.999% purity) gas up to the desired pressure $p_{C_2H_4}$ between 2×10^{-7}
89 Torr and 2×10^{-4} Torr set using a UHV leak valve. Subsequently, Ar (99.999% purity) gas is let
90 in and the total pressure is adjusted to 10 mTorr. Zr-C thin films are deposited using Zr target
91 power maintained constant at 50 W for 30 minutes. The target voltage increases with increasing
92 $p_{C_2H_4}$ from 225 V (2×10^{-7} Torr) to 227 V (2×10^{-6} Torr and 2×10^{-5} Torr), and 234 V (2×10^{-4}
93 Torr). Prior to deposition, the Zr target is sputter-cleaned using the same Ar/ C_2H_4 composition as
94 that used for the film growth for 2 minutes with the sample rotated out-of-sight from the target.
95 After deposition, the ethylene and Ar gas supplies are shut off and the chamber is evacuated
96 while the sample is passively cooled to room temperature by switching off the current supplied to
97 the substrate heater.

98 XRD 2θ - ω data are obtained following the procedure described in Ref. [34] using a Jordan
99 Valley D1 diffractometer with a sealed copper X-ray tube source, a MaxFlux specular mirror to
100 produce a parallel beam, a two bounce channel-cut (2 2 0) Si collimator crystal to select the Cu
101 $K_{\alpha 1}$ wavelength ($\lambda = 0.154056$ nm) for the incident beam, and a two bounce channel-cut (2 2 0)
102 Si analyzer crystal for the third axis optics. The sample and stage are calibrated with respect to ω ,

103 ϕ (out-of-plane rotation perpendicular to ω), and χ (in-plane rotation) about the MgO(004) peak,
104 $2\theta = 94.0496^\circ$. 2θ - ω scans for 2θ values between 20° and 100° are acquired using double-axis
105 diffraction with a step size of 0.02° and a dwell time of 1 s.

106 Cross-sectional TEM (XTEM) samples are prepared using 30 kV Ga⁺ ions in an FEI Nova
107 600 NanoLab DualBeam™ scanning electron microscope equipped with a focused ion beam
108 (FIB) source. Prior to milling, the film surface is protected by ~ 150 nm and ~ 1 μ m thick Pt
109 layers deposited sequentially, first using electron beams to minimize any damage that may incur
110 during the subsequent ion-beam-assisted deposition of the thicker layers. TEM images of the film
111 and the film-substrate interface are acquired in an FEI Titan 80-300 kV scanning TEM (S/TEM)
112 operated at 300 kV for imaging.

113 XPS data are obtained using a Kratos Analytical AXIS Ultra DLD at binding energies
114 between 0 and 1200 eV with a pass energy of 160 eV, step size of 1.0 eV, and dwell time of 0.1 s.
115 High-resolution Zr 3*d* and C 1*s* spectra are acquired using a pass energy of 20 eV and a step size
116 of 0.1 eV over the energy ranges 160 – 215 eV and 264 – 300 eV, respectively, with dwell times
117 of 0.5 s and 2 s. In order to accurately determine the bulk composition and minimize the
118 contribution to the XPS signal from surface contamination, the XPS data are obtained after Ar⁺
119 ion etching of all but one samples for 1 h and the other sample (grown using $p_{\text{C}_2\text{H}_4} = 2 \times 10^{-7}$ Torr
120 and $T_s = 923$ K) for 2.5 h. The relative concentrations of Zr and C in the films are determined
121 from the ratios of the high-resolution Zr 3*d* and C 1*s* spectral peak areas, measured using
122 CasaXPS software and defined with a Shirley background type [35], corrected by their respective
123 relative sensitivity factors, 2.58 and 0.278. In order to assess the accuracy of our quantification
124 procedure, we acquired both XPS and Rutherford backscattering spectrometry (RBS) data (details
125 below) from the same ZrC_{*x*} film (sputter-deposited on Al₂O₃(0001) using a ZrC target [36]. From

126 the XPS measurements, following the procedure described above, we determined the film
127 composition as $C/Zr = 1.44$, while the RBS analysis yielded $C/Zr = 2.04$. The apparent
128 discrepancy in the carbon contents measured using these two techniques could be due to
129 preferential removal of C from the surface during sputter-etching of the samples prior to XPS
130 measurements coupled with the fact that XPS is a surface-sensitive technique while RBS probes
131 the entire cross-section of the film.

132 RBS-Nuclear Reaction Analysis (RBS-NRA) data, used to determine the film stoichiometry
133 of one sample apart from the set of samples presented in this article, are obtained using 1.2 MeV
134 deuteron beam generated by the nuclear microprobe of CEA Saclay, France. The incident
135 deuteron beam size is $4 \times 3 \mu\text{m}^2$. Backscattered particles produced from nuclear reactions are
136 detected with an annular surface barrier particle detector (detection angle 170°). C concentrations
137 are measured from the peak of the nuclear reaction $^{12}\text{C}(d,p_0)^{13}\text{C}$ and Zr concentration from that of
138 backscattered deuterons. The film composition is deduced by fitting experimental data with
139 simulated spectra using SIMNRA code [37], which takes into account experimental beam
140 conditions and related cross-sections of scattering and deuteron induced nuclear reactions.

141

142 **3. Results and discussion**

143 Figure 1a shows XRD 2θ - ω scans acquired from Zr-C/MgO(001) samples (open circles)
144 grown at $T_s = 923$ K using Ar/C₂H₄ gas mixtures with $p_{\text{C}_2\text{H}_4}$ between 2×10^{-7} Torr and 2×10^{-4}
145 Torr. In Fig. 1a, the solid line is an experimental XRD 2θ - ω scan of a bare MgO(001) substrate,
146 provided as a reference. The higher intensity peaks at $2\theta = 42.9^\circ$ and 41.0° labeled with asterisks
147 (*) correspond to 002 reflections of the MgO single-crystal substrate due to Cu $K_{\alpha 1}$ ($\lambda = 0.154056$
148 nm) and unintentional W L_{α} ($\lambda = 0.147635$ nm) radiations from the X-ray source, respectively.

149 XRD data obtained from the layers deposited using the lowest $p_{\text{C}_2\text{H}_4}$ ($= 2 \times 10^{-7}$ Torr) do not
150 show any peaks due to B1-ZrC but reveal reflections at 2θ values corresponding to hcp Zr 0002
151 and $10\bar{1}1$. The lattice constants ($a_{\text{Zr}}, c_{\text{Zr}}$) determined from the XRD data are (0.325 ± 0.003 nm,
152 0.517 ± 0.003 nm), which are within the measurement uncertainties the same as (0.323 nm, 0.515
153 nm) of pure Zr [38]. In the same XRD pattern, we also note the presence of seemingly high
154 background intensity at $2\theta \approx 35^\circ$, highlighted by a dotted circle, between the Zr 0002 and Zr $10\bar{1}1$
155 peaks. We suggest and provide supporting evidence in the following section that this result is
156 likely due to the formation of hexagonal-structured carbides, e.g., Zr_3C_2 (P3₁21, space group 152;
157 $a_1 = 0.306$ nm and $c_1 = 1.491$ nm), whose $10\bar{1}2$ and 0006 reflections are at $2\theta = 35.9^\circ$ and 36.1° ,
158 respectively. At higher $p_{\text{C}_2\text{H}_4}$ ($= 2 \times 10^{-6}$ Torr and 2×10^{-5} Torr), the XRD data reveal peaks
159 corresponding to 002 and 111 reflections of B1-structured ZrC_x . We observe a shift in ZrC_x 111
160 reflection peak position to lower 2θ values, i.e., 111 interplanar spacing d_{111} increases, with
161 increasing $p_{\text{C}_2\text{H}_4}$ from $2\theta = 33.12^\circ$ ($d_{111} = 0.270$ nm) at 2×10^{-6} Torr to $2\theta = 32.84^\circ$ ($d_{111} = 0.273$
162 nm) at 2×10^{-5} Torr. (The 002 reflections are too broad to accurately measure any variations in
163 their peak positions and therefore we are unable to determine the existence, if any, of
164 inhomogeneous distortions in the ZrC lattice.) From the measured d_{111} values at each $p_{\text{C}_2\text{H}_4}$, we
165 determine $a = 0.468 \pm 0.004$ nm at 2×10^{-6} Torr and 0.472 ± 0.004 nm at 2×10^{-5} Torr. The
166 former is, within the measurements uncertainties, the same as $a_0 = 0.4693$ nm of the bulk
167 stoichiometric ZrC [1], while the latter is $\sim 0.6\%$ larger than a_0 , likely due to distortion of the ZrC
168 lattice due to increased incorporation of C in the films [6,13,26,27]. Similar shifts in XRD peak
169 positions have been previously observed with increasing carbon contents in sputter-deposited ZrC
170 [13], HfC [26], and NbC [27] thin films. The XRD scan from the sample grown with the highest
171 $p_{\text{C}_2\text{H}_4}$ ($= 2 \times 10^{-4}$ Torr) does not show any peaks, suggesting that the film is X-ray amorphous.

172 Based on the data in Fig. 1a, we identify $p_{\text{C}_2\text{H}_4} = 2 \times 10^{-6}$ Torr as the optimal ethylene partial
173 pressure for the growth of B1-ZrC at $T_s = 923$ K in our deposition system.

174 We investigated the effect of T_s , another key parameter that can influence the crystallinity of
175 sputter-deposited films [13,39]. Fig. 1b shows XRD data obtained from Zr-C layers sputter-
176 deposited at $723 \text{ K} \leq T_s \leq 1123 \text{ K}$ using Ar/C₂H₄ gas mixtures with $p_{\text{C}_2\text{H}_4} = 2 \times 10^{-6}$ Torr. At all
177 $T_s \leq 1023$ K, we observe two sets of peaks corresponding to B1-structured ZrC_x 111 reflection at
178 2θ values between 32.92° and 33.14° , and 002 reflection at around 38.52° . The lattice parameters
179 extracted from the 002 reflection are $\sim 0.5\%$ smaller compared to a_o of stoichiometric ZrC [1],
180 while those determined from the 111 reflections are $\sim 0.3\%$ larger (for $2\theta = 32.92^\circ$) and $\sim 0.3\%$
181 smaller (for $2\theta = 33.14^\circ$) than a_o . The peaks are however too broad and weak in intensity to
182 accurately determine the temperature-dependent variations, if any, in the carbon content x , grain
183 size, and strain. Interestingly, the XRD data obtained from the ZrC_x film grown at the highest $T_s =$
184 1123 K showed only one peak corresponding to 002 reflection, indicating that 002 texture is
185 preferred at higher T_s . These results suggest that, in our experiments, 111 texture is promoted in
186 sputter-deposited ZrC_x at lower T_s , a likely consequence of kinetic limitations inherent to the
187 deposition process. Similar T_s -dependent 111 texture evolution has been reported in a variety of
188 sputter-deposited TMC thin films [13,28,39–41].

189 We now present the microstructures of Zr-C layers sputter-deposited as a function of $p_{\text{C}_2\text{H}_4}$
190 and T_s . Figs. 2a-d are typical XTEM images obtained from the Zr-C thin films grown at $T_s = 923$
191 K using $p_{\text{C}_2\text{H}_4} =$ a) 2×10^{-7} Torr, b) 2×10^{-6} Torr, c) 2×10^{-5} Torr, and d) 2×10^{-4} Torr. We find
192 that the film thickness increases with increasing $p_{\text{C}_2\text{H}_4}$ from 87 ± 4 nm at $p_{\text{C}_2\text{H}_4} = 2 \times 10^{-7}$ Torr to
193 245 ± 20 nm at $p_{\text{C}_2\text{H}_4} = 2 \times 10^{-4}$ Torr. (This is in contrast with the results reported in Ref. [13],

194 where the deposition rate decreases with increasing reactive gas (methane) partial pressure.) We
195 attribute this result to the increase in the carbon content (supporting evidence provided in the
196 following section) within the films with increasing $p_{\text{C}_2\text{H}_4}$ during sputter-deposition. The TEM
197 images of Zr-C sample deposited using $p_{\text{C}_2\text{H}_4} = 2 \times 10^{-7}$ Torr reveal that the film is dense with
198 smooth surface and compositionally-abrupt film-substrate interface (see Fig. 2a); these results are
199 in striking contrast with the interfacial reactions observed during sputter-deposition of pure Zr
200 films on $\text{Al}_2\text{O}_3(0001)$ [33]. Lattice-resolved TEM image (for example, Fig. 2a') and
201 corresponding Fourier transform (FT) (inset in Fig. 2a') show that the Zr-C layers deposited with
202 the lowest $p_{\text{C}_2\text{H}_4} = 2 \times 10^{-7}$ Torr are crystalline and that the layer is primarily composed of hcp-
203 structured Zr. We have also observed additional reflections that we attribute to trigonal- Zr_3C_2
204 $000\bar{3}$, the presence of which could explain the observed high background XRD intensity at $2\theta \approx$
205 35° in Fig. 1a. This result suggests the coexistence of hcp-Zr and trigonal Zr_3C_2 . Increasing $p_{\text{C}_2\text{H}_4}$
206 to 2×10^{-6} Torr and 2×10^{-5} Torr leads to porous films with dendritic columns and faceted
207 surfaces (Figs. 2b and c). The corresponding higher resolution XTEM images in Figs. 2b' and c'
208 reveal regions with diffraction contrast indicative of crystallinity; surrounding regions without
209 such contrast are likely composed of amorphous C. FTs in Figs. 2b' and c' reveal reflections
210 corresponding to B1-structured 002 and 111 grains in the films, consistent with the XRD results.
211 FTs (not shown here) of the XTEM images acquired from the regions near the film-substrate
212 interfaces in these two samples reveal two sets of identical reflections, indicative of cube-on-cube
213 epitaxial growth of 002-oriented ZrC layers on the $\text{MgO}(001)$ substrate. At the highest $p_{\text{C}_2\text{H}_4} = 2$
214 $\times 10^{-4}$ Torr used in our experiments, the layers appear to be dense (see Fig. 2d). The XTEM
215 image in Fig. 2d' lacks any diffraction contrast and the corresponding FT shows a broad diffuse
216 ring, commonly associated with amorphous samples. These observations suggest that the Zr-C

217 films deposited using 2×10^{-4} Torr ethylene are amorphous and are consistent with the XRD data
218 (Fig. 1a).

219 Figs. 3a-d and 3a'-d' are series of low-magnification and higher-resolution XTEM images,
220 respectively, obtained from near the substrate-film interfaces in the $\text{ZrC}_x/\text{MgO}(001)$ samples
221 grown using $p_{\text{C}_2\text{H}_4} = 2 \times 10^{-6}$ Torr at different T_s . All the TEM images reveal fully dense layers
222 with columnar grains and corrugated surfaces, indicating that the growth morphologies and
223 microstructures are qualitatively similar in all the samples grown at different T_s . XTEM images
224 (not shown here) obtained along the growth direction also reveal the presence of amorphous
225 regions throughout the films. These results are qualitatively similar to those reported in previous
226 studies [3]. Diffraction spots corresponding to both ZrC_x 002 and 111 reflections are observed in
227 the FTs in Figs. 3a'-c', indicating that the films are polycrystalline. The FT in Fig. 3d' shows only
228 002 reflections due to B1- ZrC_x , consistent with the XRD data in Fig. 1b. From the ZrC 002
229 reflections, we extract a values ($= 0.47 \pm 0.01$ nm), $\sim 0.5\%$ smaller compared to a_o , and are
230 consistent with the value determined from the XRD data. High-resolution TEM images along
231 with their corresponding FTs (not shown here) of all samples show the presence of only 002-
232 oriented ZrC grains at the interface with a cube-on-cube relation with respect to the $\text{MgO}(001)$
233 substrate, indicative of heteroepitaxial growth during the early stages of deposition.

234 In order to quantify the free and the bonded carbon contents in ZrC_x in the films, we used
235 XPS. Fig. 4a shows representative high-resolution C 1s and Zr 3d XPS data acquired from the
236 bulk of Zr-C samples grown using different $p_{\text{C}_2\text{H}_4}$. Within these spectra, we identify peaks
237 associated with carbon at binding energies: 284.0 ~ 284.2 eV as C-C bonds in free-carbon; 281.2
238 ~ 282 eV as C-Zr bonds; and 282 ~ 284 eV as C-Zr* bonds [3,5,42,43]. The XPS peak due to C-
239 C bond in carbides is often attributed to the presence of disordered, sp^2 (graphite), and/or sp^3

240 (diamond) hybridized carbon, whose exact contributions to the XPS signal are not resolvable in
241 our measurements [6,44]. The peaks observed at binding energies between 178.1 and 180.5 eV
242 correspond to Zr $3d_{5/2}$ and Zr $3d_{3/2}$, respectively. We find that the Zr peaks are better defined at
243 lower $p_{C_2H_4}$ than at higher values, presumably due to the decrease in free-C content. With
244 increasing $p_{C_2H_4}$, we observe a shift (compared to the dashed vertical lines in the plot, which
245 correspond to binding energies in stoichiometric ZrC) in the C-Zr and Zr $3d$ peak positions to
246 higher binding energies. Based on the increase in C-C, and concomitant decrease in the C-Zr,
247 peak intensities with increasing $p_{C_2H_4}$, we suggest that the observed peak shifts are due to the
248 increase in free-C content in the films.

249 From the measurements of the Zr $3d$, C-C, C-Zr, and C-Zr* peak areas from Fig. 4a, we
250 quantify the concentrations of total carbon, free-C, and bonded-carbon x in ZrC_x , plotted as
251 magenta, black, and green curves, respectively, as a function of $p_{C_2H_4}$ in Fig. 4b. The label free-C
252 in the plot refers to the elemental carbon that is not bonded to Zr and corresponds to C-C peaks in
253 Fig. 4a. We find that the amount of total C and free-C increase while the fraction of carbon
254 bonded to Zr, i.e. the carbide phase, decreases with increasing $p_{C_2H_4}$ during sputter-deposition.
255 These results are consistent with the observation of increasing fraction of amorphous phase with
256 increasing $p_{C_2H_4}$ in the TEM images in Fig. 2 and are commonly observed in sputter-deposited
257 Zr-C films [3]. Interestingly, the fraction of free-C relative to the amount of carbon in the carbide
258 phase is higher in our films than in the films deposited using three orders of magnitude higher
259 reactive gas (methane) partial pressure [3]. Possible reasons for this behavior include: differences
260 in the rates of dissociative chemisorption of carbon due to precursor composition (relatively more
261 stable methane with one C atom/molecule vs. ethylene with two C atoms/molecule), Zr
262 deposition rates, T_s , total gas pressure, plasma characteristics, and residual gas composition and

263 concentration. Among all these samples, based on the XPS data, we note that the films deposited
264 using $p_{\text{C}_2\text{H}_4} = 2 \times 10^{-6}$ Torr yield the highest fraction of Zr-C phase with the least amount of free-
265 C. In the following section, we present the effect of T_s on the composition of Zr-C films deposited
266 with $p_{\text{C}_2\text{H}_4} = 2 \times 10^{-6}$ Torr.

267 Fig. 4c shows representative C 1s and Zr 3d spectra obtained from the Zr-C samples grown
268 at different T_s using $p_{\text{C}_2\text{H}_4} = 2 \times 10^{-6}$ Torr. From the spectra, we identify the two characteristic Zr
269 $3d_{5/2}$ and $3d_{3/2}$ peaks. In the C 1s spectra, we observe one high intensity peak at ~ 281 eV, which
270 we attribute to C-Zr bonds, and one relatively broader peak around 284 eV due to C-C bonds.
271 With increasing T_s , we observe shifts (~ 0.3 eV) in both the Zr 3d and C-Zr peaks to higher
272 binding energies, suggestive of stronger bonding presumably due to decrease in the C-content
273 within the carbide; the magnitude of shift is more pronounced at higher T_s (≥ 923 K). In all the
274 samples grown at different T_s , C-C peaks are broad, shallow, and changes (if any) in the peak
275 positions are not detectable. The T_s -dependent changes in total C, free-C, and bonded-carbon
276 concentrations are plotted in Fig. 4d. We find that the amounts of total C (magenta curve) and
277 free-C (black curve) increase marginally with increasing T_s , indicating that substrate temperatures
278 over 723 K have little influence on the total C and free-C contents in the Zr-C films sputter-
279 deposited using $p_{\text{C}_2\text{H}_4} = 2 \times 10^{-6}$ Torr. (These results are opposite to those reported for Zr-C films
280 sputter-deposited using methane gas [13], which as mentioned earlier could be not only due to the
281 use of ethylene vs. methane but also system-specific deposition parameters.) Based on these
282 results, we suggest that during reactive sputter-deposition of Zr using low ethylene partial
283 pressures, such as $p_{\text{C}_2\text{H}_4} = 2 \times 10^{-6}$ Torr, incorporation of C from C_2H_4 into the growing films
284 occurs readily at all $T_s \geq 723$ K.

285

286 **4. Conclusions**

287 This report presents the effects of ethylene partial pressure ($p_{\text{C}_2\text{H}_4}$) and substrate temperature
288 (T_s) on the microstructural and compositional evolution of reactively sputter-deposited Zr-C thin
289 films on MgO(001) substrates using ultra-high vacuum dc magnetron sputtering of Zr target in
290 Ar/C₂H₄ gas mixtures with fairly low $p_{\text{C}_2\text{H}_4} \leq 2\%$ of the total pressure. We find that all the Zr-C
291 films, irrespective of the $p_{\text{C}_2\text{H}_4}$ and T_s , are polycrystalline two-phase mixtures composed of
292 hexagonal close-packed Zr:C solid solutions (at ultra-low $p_{\text{C}_2\text{H}_4} = 0.002\%$) or B1-ZrC_x (at higher
293 $p_{\text{C}_2\text{H}_4}$) and free-C. The amount of free-C incorporated into the films depends sensitively on $p_{\text{C}_2\text{H}_4}$
294 at $T_s = 923$ K. Increasing the T_s above 723 K (with $p_{\text{C}_2\text{H}_4} = 2 \times 10^{-6}$ Torr) has little effect on the
295 carbon incorporation rate. Our results indicate that relatively small amount of ethylene gas
296 (0.02% of the total pressure in our experiments) is sufficient to deposit two-phase mixtures of
297 ZrC and free-carbon. Given that pure, single-phase carbide films are often desirable, we suggest
298 that reactive sputter-deposition of ZrC (and other TMC) films is probably best carried out using
299 ultra-low partial pressures of carbon containing precursors; the exact pressure however depends
300 on the deposition system, substrate temperature, deposition rate, and the precursor.

301

302 **Acknowledgements**

303 We gratefully acknowledge support from the Air Force Office of Scientific Research (AFOSR,
304 Dr. Ali Sayir) under Grant # FA9550-14-1-0106 and # FA9550-18-1-0050. We thank the Office
305 of Naval Research (Dr. Chagaan Baatar) for the funds received under Grant #N00014-12-1-0518
306 used to build the UHV deposition system. KT is supported by the Japanese Student Service
307 Organization (L16111111026) and the UCLA department of materials science and engineering
308 for his doctoral study in the United States. AA is supported by the National Science Foundation

309 (NSF CMMI) grant #1563427 (Dr. Kara Peters). We thank Mr. Noah Bodzin and the
310 Nanoelectronics Research Facility in the UCLA Henry Samueli School of Engineering for
311 assistance with focused ion beam milling and acknowledge the use of instruments at the Electron
312 Imaging Center for NanoMachines supported by NIH (1S10RR23057) and the California
313 NanoSystems Institute at UCLA.

314 **References**

- 315 [1] M. Morris, E.H. Evans, H.S. Parker, W. Wong-Ng, D.M. Gladhill, C.R. Hubbard, Standard
316 x-ray diffraction powder patterns, National Bureau of Standards, 1984.
317 <http://archive.org/details/standardxraydiff2521morr> (accessed March 18, 2019).
- 318 [2] H.O. Pierson, Handbook of Refractory Carbides and Nitrides: Properties, Characteristics,
319 Processing and Applications, Elsevier Science, New Jersey, USA, 1996.
- 320 [3] Q.N. Meng, M. Wen, F. Mao, N. Nedfors, U. Jansson, W.T. Zheng, Deposition and
321 characterization of reactive magnetron sputtered zirconium carbide films, Surface and
322 Coatings Technology. 232 (2013) 876–883. <https://doi.org/10.1016/j.surfcoat.2013.06.116>.
- 323 [4] S. Norgren, J. García, A. Blomqvist, L. Yin, Trends in the P/M hard metal industry,
324 International Journal of Refractory Metals and Hard Materials. 48 (2015) 31–45.
325 <https://doi.org/10.1016/j.ijrmhm.2014.07.007>.
- 326 [5] M. Andersson, S. Urbonaite, E. Lewin, U. Jansson, Magnetron sputtering of Zr–Si–C thin
327 films, Thin Solid Films. 520 (2012) 6375–6381. <https://doi.org/10.1016/j.tsf.2012.06.044>.
- 328 [6] L.E. Toth, Transition metal carbides and nitrides, Academic Press, 1971.
- 329 [7] J. Balko, T. Csanádi, R. Sedlák, M. Vojtko, A. Kovalíková, K. Koval, P. Wyzga, A.
330 Naughton-Duszová, Nanoindentation and tribology of VC, NbC and ZrC refractory
331 carbides, Journal of the European Ceramic Society. 37 (2017) 4371–4377.
332 <https://doi.org/10.1016/j.jeurceramsoc.2017.04.064>.
- 333 [8] F. Monteverde, A. Bellosi, L. Scatteia, Processing and properties of ultra-high temperature
334 ceramics for space applications, Materials Science and Engineering: A. 485 (2008) 415–
335 421. <https://doi.org/10.1016/j.msea.2007.08.054>.
- 336 [9] K. Minato, T. Ogawa, K. Fukuda, H. Nabielek, H. Sekino, Y. Nozawa, I. Takahashi, Fission
337 product release from ZrC-coated fuel particles during postirradiation heating at 1600°C,
338 Journal of Nuclear Materials. 224 (1995) 85–92. [https://doi.org/10.1016/0022-3115\(95\)00032-1](https://doi.org/10.1016/0022-3115(95)00032-1).
- 340 [10] S. Ueta, J. Aihara, A. Yasuda, H. Ishibashi, T. Takayama, K. Sawa, Fabrication of uniform
341 ZrC coating layer for the coated fuel particle of the very high temperature reactor, Journal of
342 Nuclear Materials. 376 (2008) 146–151. <https://doi.org/10.1016/j.jnucmat.2008.02.068>.
- 343 [11] Y. Katoh, G. Vasudevamurthy, T. Nozawa, L.L. Snead, Properties of zirconium carbide for
344 nuclear fuel applications, Journal of Nuclear Materials. 441 (2013) 718–742.
345 <https://doi.org/10.1016/j.jnucmat.2013.05.037>.
- 346 [12] W.A. Mackie, P.R. Davis, Single-crystal zirconium carbide as a high-temperature
347 thermionic cathode material, IEEE Transactions on Electron Devices. 36 (1989) 220–224.
348 <https://doi.org/10.1109/16.21209>.
- 349 [13] J. Brückner, T. Mäntylä, Reactive magnetron sputtering of zirconium carbide films using
350 Ar-CH₄ gas mixtures, Surface and Coatings Technology. 59 (1993) 166–170.
351 [https://doi.org/10.1016/0257-8972\(93\)90077-2](https://doi.org/10.1016/0257-8972(93)90077-2).
- 352 [14] J. Xu, S. Jiang, Y. Wang, S. Shang, D. Miao, R. Guo, Photo-thermal conversion and thermal
353 insulation properties of ZrC coated polyester fabric, Fibers Polym. 18 (2017) 1938–1944.
354 <https://doi.org/10.1007/s12221-017-1237-z>.
- 355 [15] X.-H. Gao, H.-X. Guo, T.-H. Zhou, G. Liu, Optical properties and failure analysis of ZrC-
356 ZrO_x ceramic based spectrally selective solar absorbers deposited at a high substrate
357 temperature, Solar Energy Materials and Solar Cells. 176 (2018) 93–99.
358 <https://doi.org/10.1016/j.solmat.2017.11.018>.

- 359 [16] M. Balden, B.T. Cieciva, I. Quintana, E. de Juan Pardo, F. Koch, M. Sikora, B. Dubiel,
360 Metal-doped carbon films obtained by magnetron sputtering, *Surface and Coatings*
361 *Technology*. 200 (2005) 413–417. <https://doi.org/10.1016/j.surfcoat.2005.02.218>.
- 362 [17] M. Dollé, D. Gosset, C. Bogicevic, F. Karolak, D. Simeone, G. Baldinozzi, Synthesis of
363 nanosized zirconium carbide by a sol–gel route, *Journal of the European Ceramic Society*.
364 27 (2007) 2061–2067. <https://doi.org/10.1016/j.jeurceramsoc.2006.06.005>.
- 365 [18] K. Minato, T. Ogawa, T. Koya, H. Sekino, T. Tomita, Retention of fission product caesium
366 in ZrC-coated fuel particles for high-temperature gas-cooled reactors, *Journal of Nuclear*
367 *Materials*. 279 (2000) 181–188. [https://doi.org/10.1016/S0022-3115\(00\)00015-5](https://doi.org/10.1016/S0022-3115(00)00015-5).
- 368 [19] G.H. Reynolds, Chemical vapor deposition of ZrC on pyrocarbon-coated fuel particles, *J.*
369 *Nucl. Mater.*, v. 50, No. 2, Pp. 215–216. (1974). [https://doi.org/10.1016/0022-](https://doi.org/10.1016/0022-3115(74)90158-5)
370 [3115\(74\)90158-5](https://doi.org/10.1016/0022-3115(74)90158-5).
- 371 [20] Y.S. Won, V.G. Varanasi, O. Kryliouk, T.J. Anderson, L. McElwee-White, R.J. Perez,
372 Equilibrium analysis of zirconium carbide CVD growth, *Journal of Crystal Growth*. 307
373 (2007) 302–308. <https://doi.org/10.1016/j.jcrysgr.2007.05.039>.
- 374 [21] V. Craciun, J. Woo, D. Craciun, R.K. Singh, Epitaxial ZrC thin films grown by pulsed laser
375 deposition, *Applied Surface Science*. 252 (2006) 4615–4618.
376 <https://doi.org/10.1016/j.apsusc.2005.07.139>.
- 377 [22] L. D'Alessio, A. Santagata, R. Teghil, M. Zaccagnino, I. Zaccardo, V. Marotta, D. Ferro, G.
378 De Maria, Zirconium carbide thin films deposited by pulsed laser ablation, *Applied Surface*
379 *Science*. 168 (2000) 284–287. [https://doi.org/10.1016/S0169-4332\(00\)00625-5](https://doi.org/10.1016/S0169-4332(00)00625-5).
- 380 [23] E. Portolan, C.L.G. Amorim, G.V. Soares, C. Aguzzoli, C.A. Perottoni, I.J.R. Baumvol,
381 C.A. Figueroa, Carbon occupancy of interstitial sites in vanadium carbide films deposited by
382 direct current reactive magnetron sputtering, *Thin Solid Films*. 517 (2009) 6493–6496.
383 <https://doi.org/10.1016/j.tsf.2009.03.202>.
- 384 [24] X. Wu, G. Li, Y. Chen, G. Li, Microstructure and mechanical properties of vanadium
385 carbide coatings synthesized by reactive magnetron sputtering, *International Journal of*
386 *Refractory Metals and Hard Materials*. 27 (2009) 611–614.
387 <https://doi.org/10.1016/j.ijrmhm.2008.09.014>.
- 388 [25] A.Z. Ait Djafer, N. Saoula, N. Madaoui, A. Zerizer, Deposition and characterization of
389 titanium carbide thin films by magnetron sputtering using Ti and TiC targets, *Applied*
390 *Surface Science*. 312 (2014) 57–62. <https://doi.org/10.1016/j.apsusc.2014.05.084>.
- 391 [26] G. Li, G. Li, Microstructure and mechanical properties of hafnium carbide coatings
392 synthesized by reactive magnetron sputtering, *J Coat Technol Res*. 7 (2010) 403–407.
393 <https://doi.org/10.1007/s11998-009-9225-x>.
- 394 [27] K. Zhang, M. Wen, G. Cheng, X. Li, Q.N. Meng, J.S. Lian, W.T. Zheng, Reactive
395 magnetron sputtering deposition and characterization of niobium carbide films, *Vacuum*. 99
396 (2014) 233–241. <https://doi.org/10.1016/j.vacuum.2013.06.012>.
- 397 [28] S.S. Kumar, A. Sharma, G.M. Rao, S. Suwas, Investigations on the effect of substrate
398 temperature on the properties of reactively sputtered zirconium carbide thin films, *Journal of*
399 *Alloys and Compounds*. 695 (2017) 1020–1028.
400 <https://doi.org/10.1016/j.jallcom.2016.10.225>.
- 401 [29] N.C. Zoita, V. Braic, M. Danila, A.M. Vlaicu, C. Logofatu, C.E.A. Grigorescu, M. Braic,
402 Influence of film thickness on the morphological and electrical properties of epitaxial TiC
403 films deposited by reactive magnetron sputtering on MgO substrates, *Journal of Crystal*
404 *Growth*. 389 (2014) 92–98. <https://doi.org/10.1016/j.jcrysgr.2013.11.076>.

- 405 [30] D.D. Kumar, N. Kumar, S. Kalaiselvam, R. Radhika, S. Dash, A.K. Tyagi, R. Jayavel,
406 Reactive magnetron sputtered wear resistant multilayer transition metal carbide coatings:
407 microstructure and tribo-mechanical properties, *RSC Adv.* 5 (2015) 81790–81801.
408 <https://doi.org/10.1039/C5RA16465F>.
- 409 [31] K. Tanaka, A. Aleman, M.E. Liao, Y. Wang, M.S. Goorsky, S. Kodambaka, Effects of ultra-
410 low ethylene partial pressure on microstructure and composition of reactively sputter-
411 deposited Ta–C thin films, *Thin Solid Films.* 688 (2019) 137440.
412 <https://doi.org/10.1016/j.tsf.2019.137440>.
- 413 [32] J. Fankhauser, M. Sato, D. Yu, A. Ebnonnasir, M. Kobashi, M.S. Goorsky, S. Kodambaka,
414 Growth and characterization of epitaxial Zr(0001) thin films on Al₂O₃(0001), *Journal of*
415 *Vacuum Science & Technology A.* 34 (2016) 050606. <https://doi.org/10.1116/1.4961452>.
- 416 [33] K. Tanaka, J. Fankhauser, H. Zaid, A. Aleman, M. Sato, D. Yu, A. Ebnonnasir, C. Li, M.
417 Kobashi, M.S. Goorsky, S. Kodambaka, Kinetics of Zr-Al intermetallic compound
418 formation during ultra-high vacuum magnetron sputter-deposition of Zr/Al₂O₃(0001) thin
419 films, *Acta Materialia.* 152 (2018) 34–40. <https://doi.org/10.1016/j.actamat.2018.04.018>.
- 420 [34] A. Aleman, C. Li, H. Zaid, H. Kindlund, J. Fankhauser, S.V. Prikhodko, M.S. Goorsky, S.
421 Kodambaka, Ultrahigh vacuum dc magnetron sputter-deposition of epitaxial
422 Pd(111)/Al₂O₃(0001) thin films, *Journal of Vacuum Science & Technology A.* 36 (2018)
423 030602. <https://doi.org/10.1116/1.5021609>.
- 424 [35] N. Fairley, A. Carrick, *Casa XPS User's Manual*, (2001).
- 425 [36] J.P. Fankhauser, *Growth and Characterization of Zr and ZrC Thin Films on Al₂O₃(0001)*,
426 UCLA, 2016. <https://escholarship.org/uc/item/6db4489v> (accessed February 15, 2020).
- 427 [37] M. Mayer, SIMNRA, a simulation program for the analysis of NRA, RBS and ERDA, *AIP*
428 *Conference Proceedings.* 475 (1999) 541–544. <https://doi.org/10.1063/1.59188>.
- 429 [38] A.I. Kolesnikov, A.M. Balagurov, I.O. Bashkin, A.V. Belushkin, E.G. Ponyatovsky, M.
430 Prager, Neutron scattering studies of ordered gamma -ZrD, *J. Phys.: Condens. Matter.* 6
431 (1994) 8977–8988. <https://doi.org/10.1088/0953-8984/6/43/004>.
- 432 [39] C. Aguzzoli, C.A. Figueroa, G.V. Soares, I.J.R. Baumvol, Physicochemical and structural
433 characteristics of TiC and VC thin films deposited by DC reactive magnetron sputtering, *J*
434 *Mater Sci.* 45 (2010) 4994–5001. <https://doi.org/10.1007/s10853-010-4364-0>.
- 435 [40] H. Colder, R. Rizk, M. Morales, P. Marie, J. Vicens, I. Vickridge, Influence of substrate
436 temperature on growth of nanocrystalline silicon carbide by reactive magnetron sputtering,
437 *Journal of Applied Physics.* 98 (2005) 024313. <https://doi.org/10.1063/1.1985975>.
- 438 [41] C.-S. Chen, C.-P. Liu, C.-Y.A. Tsao, Influence of growth temperature on microstructure and
439 mechanical properties of nanocrystalline zirconium carbide films, *Thin Solid Films.* 479
440 (2005) 130–136. <https://doi.org/10.1016/j.tsf.2004.11.196>.
- 441 [42] A. Escudeiro, N.M. Figueiredo, T. Polcar, A. Cavaleiro, Structural and mechanical
442 properties of nanocrystalline Zr co-sputtered a-C(:H) amorphous films, *Applied Surface*
443 *Science.* 325 (2015) 64–72. <https://doi.org/10.1016/j.apsusc.2014.11.015>.
- 444 [43] U. Jansson, E. Lewin, Sputter deposition of transition-metal carbide films — A critical
445 review from a chemical perspective, *Thin Solid Films.* 536 (2013) 1–24.
446 <https://doi.org/10.1016/j.tsf.2013.02.019>.
- 447 [44] R. Blume, D. Rosenthal, J.-P. Tessonier, H. Li, A. Knop-Gericke, R. Schlögl,
448 *Characterizing Graphitic Carbon with X-ray Photoelectron Spectroscopy: A Step-by-Step*
449 *Approach*, *ChemCatChem.* 7 (2015) 2871–2881. <https://doi.org/10.1002/cctc.201500344>.
- 450

451 **List of Figures**

452

453 **Fig. 1.** 2θ - ω X-ray diffraction (XRD) data obtained from Zr-C/MgO(001) samples sputter-
454 deposited in 10 mTorr Ar/C₂H₄ gas mixtures at (a) $T_s = 923$ K with 2×10^{-7} Torr $\leq p_{\text{C}_2\text{H}_4} \leq 2 \times$
455 10^{-4} Torr and (b) 723 K $\leq T_s \leq 1123$ K using $p_{\text{C}_2\text{H}_4} = 2 \times 10^{-6}$ Torr. An XRD scan of MgO(001)
456 substrate (solid line) is plotted as a reference. The peaks labeled with * denote MgO 002
457 reflections due to Cu K α at $2\theta = 42.9^\circ$ and W L α at $2\theta = 40.94^\circ$. The vertical dashed lines
458 identify the 111 and 002 reflections in stoichiometric B1-ZrC and 0002 and $10\bar{1}1$ reflections in
459 hcp-Zr. The dotted circle highlights the high background intensity at $2\theta \sim 35^\circ$.

460

461 **Fig. 2.** Typical bright-field cross-sectional transmission electron microscopy (XTEM) images of
462 Zr-C/MgO(001) samples grown at $T_s = 923$ K with $p_{\text{C}_2\text{H}_4} =$ (a) 2×10^{-7} Torr, (b) 2×10^{-6} Torr, (c)
463 2×10^{-5} Torr, and (d) 2×10^{-4} Torr. (a'-d') Higher resolution XTEM images of the samples in (a-
464 d), respectively. The insets are the Fourier transforms (FTs) of the images in a'-d'. Cyan, purple,
465 red, and green circles highlight Zr 0002, Zr₃C₂ 000 $\bar{3}$, ZrC 002, and ZrC 111 reflections,
466 respectively. The absence of any spots in the Fig. 2d' FT implies that the region within the field of
467 view is likely amorphous.

468

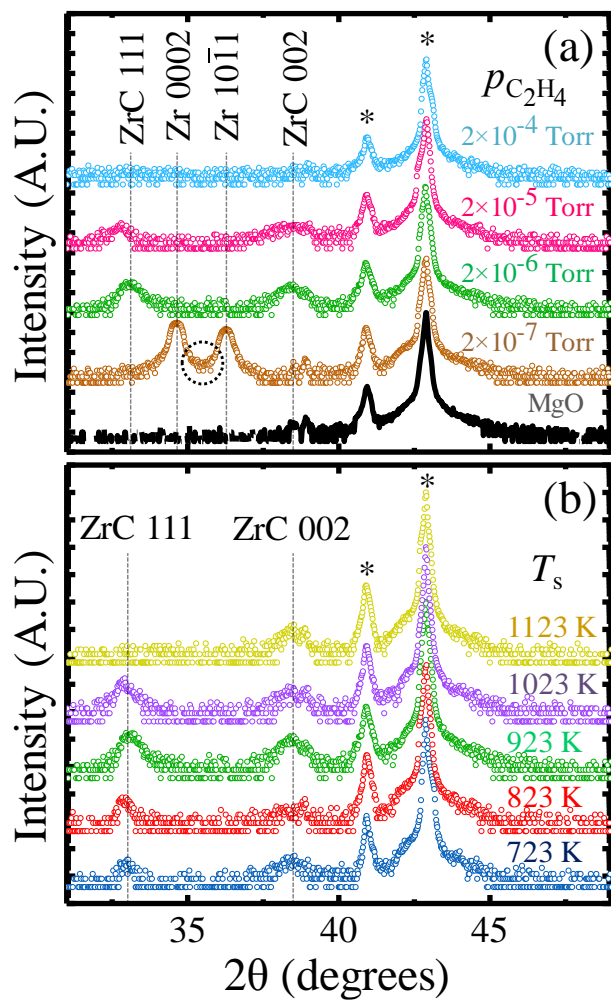
469 **Fig. 3.** Bright-field XTEM images of Zr-C/MgO(001) samples sputter-deposited using $p_{\text{C}_2\text{H}_4} = 2$
470 $\times 10^{-6}$ Torr at $T_s =$ (a) 723 K, (b) 823 K, (c) 1023 K, and (d) 1123 K. All the samples appear
471 dense with columnar microstructures and smoother surfaces. (a'-d') Representative higher-
472 resolution XTEM images with corresponding FTs as insets of the samples in (a-d), respectively.

473 All the TEM images show crystalline and amorphous regions. ZrC 002 and 111 reflections are
474 highlighted using red and green circles in the FTs, respectively.

475 **Fig. 4.** (a) X-ray photoelectron spectroscopy (XPS) data acquired around Zr 3d (175 – 190 eV)
476 and C 1s (279 – 288 eV) from sputter-etched Zr-C samples deposited as a function of $p_{C_2H_4}$. (b)
477 Total, free, and bonded carbon concentrations extracted from the XPS data plotted as a function
478 of $p_{C_2H_4}$. (c) XPS data of sputter-etched Zr-C samples deposited as a function of T_s . (d) Plot of
479 total, free, and bonded carbon concentrations vs. T_s . In both (a) and (c), the dashed vertical lines
480 correspond to binding energies in stoichiometric ZrC; black, purple, and light magenta curves
481 correspond to C-C, C-Zr, and C-Zr* components, respectively. In the plots (b) and (d), magenta,
482 black, and green curves represent the total C, free-C, and bonded carbon (labeled 'C in Zr-C')
483 contents in the Zr-C samples, respectively.

484

485

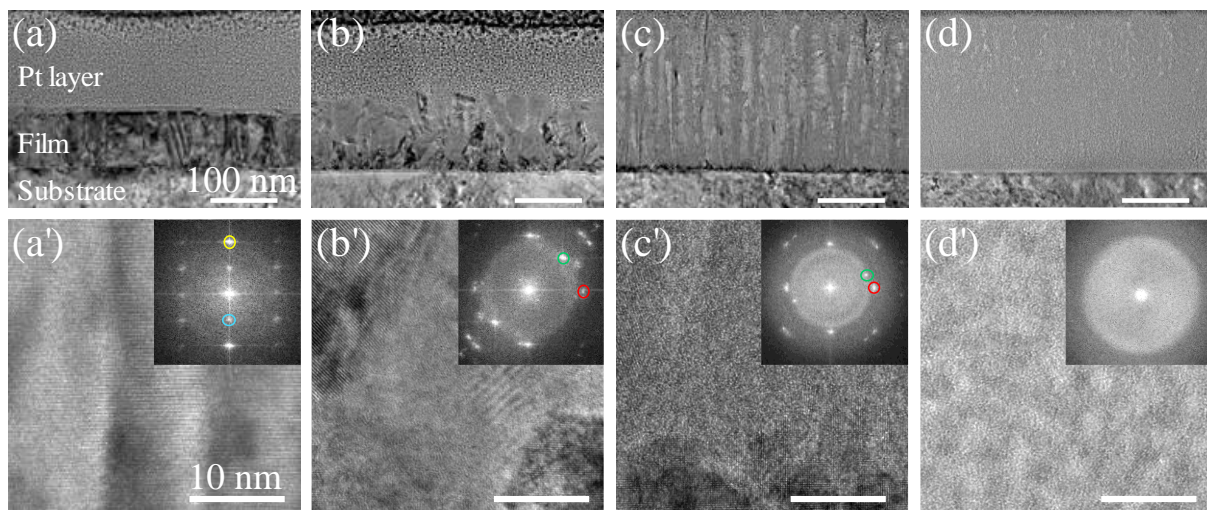


486

487 **Figure 1**

488

489

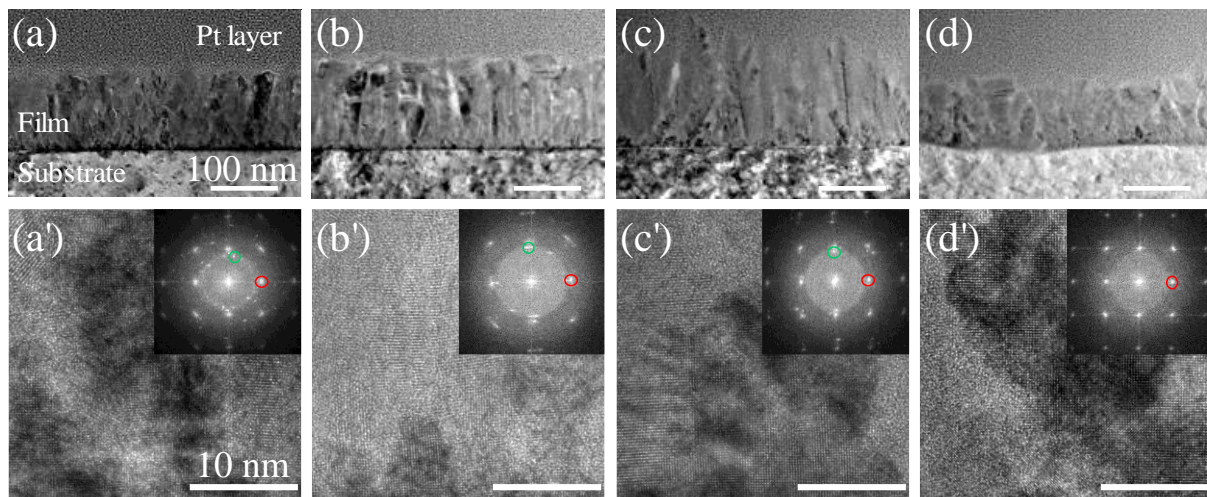


490

491 **Figure 2**

492

493



494

495 **Figure 3**

496

